Journal of Energy Chemistry 105 (2025) 35–43

Contents lists available at ScienceDirect

Journal of Energy Chemistry

journal homepage: www.elsevier.com/locate/jechem

http://www.journals.elsevier.com/journal-of-energy-chemistry/

Tailoring anion-dominant solvation environment by steric-hindrance effect and competitive coordination for fast charging and stable cycling lithium metal batteries

Ruizhe Xu [a], Anjun Hu [a,e,*], Zhen Wang [a], Kai Chen [a], Jingze Chen [a], Wang Xu [a], Gang Wu [d], Fei Li [c,*], Jian Wang [b,f,*], Jianping Long [a,*]

[a] College of Materials and Chemistry & Chemical Engineering, Chengdu University of Technology, Chengdu Sichuan, 610059, China
[b] Helmholtz Institute Ulm (HIU), D89081 Ulm, Germany
[c] School of Materials and Energy, University of Electronic Science and Technology of China, Chengdu Sichuan, 610054, China
[d] The Collaborative Innovation Center for Eco-Friendly and Fire-Safety Polymeric Materials (MoE), National Engineering Laboratory of Eco-Friendly Polymeric Materials (Sichuan), State Key Laboratory of Polymer Materials Engineering, College of Chemistry, Sichuan University, Chengdu Sichuan, 610064, China
[e] Lithium Resources and Lithium Materials Key Laboratory of Sichuan Province, Chengdu Sichuan, 610059, China
[f] Karlsruhe Institute of Technology (KIT), Karlsruhe D-76021, Germany

ARTICLE INFO

Article history:
Received 12 December 2024
Revised 15 January 2025
Accepted 15 January 2025
Available online 11 February 2025

Keywords:
Lithium metal batteries
Fast charging
Stable cycling
Solvation structure

ABSTRACT

The properties of electrolytes are critical for fast-charging and stable-cycling applications in lithium metal batteries (LMBs). However, the slow kinetics of Li^+ transport and desolvation in commercial carbonate electrolytes, coupled with the formation of unstable solid electrolyte interphases (SEI), exacerbate the degradation of LMB performance at high current densities. Herein, we propose a versatile electrolyte design strategy that incorporates cyclohexyl methyl ether (CME) as a co-solvent to reshape the Li^+ solvation environment by the steric-hindrance effect of bulky molecules and their competitive coordination with other solvent molecules. Simulation calculations and spectral analysis demonstrate that the addition of CME molecules reduces the involvement of other solvent molecules in the Li^+ solvation sheath and promotes the formation of Li^+–PF_6^- coordination, thereby accelerating Li^+ transport kinetics. Additionally, this electrolyte composition improves Li^+ desolvation kinetics and fosters the formation of inorganic-rich SEI, ensuring cycle stability under fast charging. Consequently, the Li||$LiNi_{0.8}Co_{0.1}Mn_{0.1}O_2$ battery with the modified electrolyte retains 82% of its initial capacity after 463 cycles at 1 C. Even under the extreme fast-charging condition of 5 C, the battery can maintain 80% capacity retention after 173 cycles. This work provides a promising approach for the development of high-performance LMBs by modulating solvation environment of electrolytes.

1. Introduction

With the rise of the electric vehicle (EV) industry, the demand for advanced battery technology has escalated, necessitating batteries with higher energy density, faster charging and longer cycle life [1–3]. While lithium-ion batteries currently dominate the market, they face limitations in meeting the growing performance demands of EV, particularly in terms of high-power output and fast charging [4]. Among the various alternative technologies, lithium metal batteries (LMBs) are considered ideal for the next-generation batteries due to the high theoretical specific capacity of lithium metal anode (3860 mA h g^{-1}) and low electrochemical potential (−3.04 V vs. standard hydrogen electrode) [5,6]. However, the use of conventional electrolytes in LMBs presents many challenges, including poor stability of solid electrolyte interphase (SEI), slow Li^+ transport and desolvation kinetics, which are particularly pronounced under high current density conditions [7–11]. Therefore, enhancing the kinetic properties of the electrolyte and the stability of the SEI is crucial for achieving high-performance batteries with long cycle life and fast charging properties [12,13].

Electrolyte is a critical component of LMBs, serving not only as a medium for ion transport but also influencing the composition and

* Corresponding authors.
E-mail addresses: anjunhu@cdut.edu.cn (A. Hu), feili@uestc.edu.cn (F. Li), jian.wang@kit.edu (J. Wang), longjianping@cdut.cn (J. Long).

https://doi.org/10.1016/j.jechem.2025.01.038

structure of the SEI [14,15]. The solvation sheath of the electrolyte directly determines the interfacial stability and electrochemical kinetics, significantly impacting the performance of LMBs [16]. In conventional electrolytes, Li^+ is surrounded by strongly solvated polar solvents, forming a large number of solvent-separated ion pairs (SSIP), leading to organic-rich SEI with high interfacial impedance limits battery performance [17,18]. To improve the solvation structure, a strategy to construct a high-concentration electrolyte (HCE) was proposed. In the HCE, more anions participate in the solvation sheath of Li^+, forming contact ion pairs (CIP) and aggregated ions (AGG), which promote anion decomposition and generate inorganic-rich SEI, thereby reducing the interfacial impedance and enhancing the rate performance of the battery [19]. However, incomplete dissociation of lithium salts in HCE leads to decreased conductivity and increased viscosity, which increases the Li^+ transport resistance [20–22]. To mitigate these issues, localized high concentration electrolyte (LHCE) have been developed by adding uncoordinated hydrofluoric ethers as diluents to HCE [23,24], but they still suffer from insufficient salts dissociation, reducing the carrier concentration during cycling and limiting the battery performance at high current densities [25]. Variety strategies, including ternary anionic electrolytes [26], fluorinated carbonate electrolytes [27], deep eutectic electrolytes [28] and high-entropy electrolytes [29,30], have been explored to modulate the solvation sheath. While these approaches show improvements, challenges remain in simultaneously achieving high ionic conductivity and anion-rich solvation sheath.

In this work, we propose a versatile electrolyte design strategy that utilizes cyclohexyl methyl ether (CME) bulky molecule with steric-hindrance effect of macromolecules and the competitive coordination between solvent molecules to tailor the solvation environment of Li^+ in conventional carbonate-based electrolytes, which realize long-cycling and fast-charging LMBs (Fig. 1). Our results show that CME molecules effectively coordinate with Li^+, and their significant steric-hindrance effect reduces the coordination strength of conventional solvents (e.g., ethylene carbonate, EC) with Li^+, making the solvation sheath of Li^+ looser. This change enhances the coordination probability between Li^+ and anions, promoting the formation of anion-rich solvation sheath and accelerating the Li^+ transport. Meanwhile, this optimized solvation sheath leads to the formation of a highly stable and inorganic-rich component SEI with fast interfacial dynamics, enabling dendrite-free lithium deposition and significantly enhancing the battery performance. As a result, the Li||$LiNi_{0.8}Co_{0.1}Mn_{0.1}O_2$ battery with the modified electrolyte retains 82% of its initial capacity after 463 cycles at 1 C. Moreover, it exhibits excellent stability under fast charging conditions, retaining 80% of its capacity after 176 cycles at a high rate of 5 C.

2. Results and discussion

2.1. Electrolyte formulation and Li^+ solvation structure

CME was selected as an electrolyte co-solvent to modulate the solvation sheath of Li^+ due to its appropriate solvation ability and significant steric-hindrance effect. In this study, four electrolytes, BE-4CME, BE-6CME, BE-8CME and BE-10CME, were prepared by adding 4 wt%, 6 wt%, 8 wt%, and 10 wt% of CME, respectively, to a commercial carbonate electrolyte consisting of 1 M $LiPF_6$ in EC/DEC (1:1 by volume, denoted as BE). As shown in Fig. 2a, the cyclohexane part of CME effectively increases the spatial occupation and reduces the possibility of EC and DEC molecules entering the solvation sheath. The steric-hindrance effect of the cyclohexane part weakens the coordination of Li^+ with the solvent molecules, thereby changing the solvation sheath of Li^+. The presence of C–O–C bond provides a coordination site for Li^+, and CME coordinates with Li^+ through C–O–C bond and enters the Li^+ solvation sheath. Given the similar binding energies of EC, DEC and CME molecules, there is no significant difference in their coordination abilities with Li^+. The addition of CME leads to competitive coordination among the three molecules, further weakening the coordination of Li^+ with EC and DEC, and favoring the entry of anions into the solvation sheath to coordinate with Li^+.

Electrostatic surface potential (ESP) calculations (Fig. 2b) using density-functional theory (DFT) reveal that the CME molecule has a strong negative electrostatic potential at the oxygen atom site on the methoxy group, indicating its enhanced ability to solvate Li^+ [31,32]. Compared with EC and DEC, the chelation of Li^+ by the

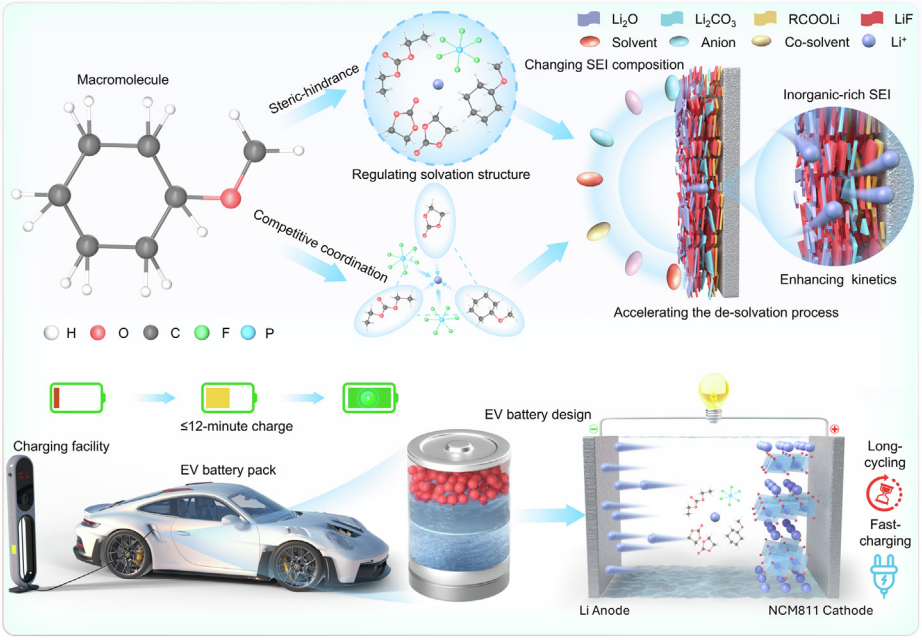

Fig. 1. The mechanism of this electrolyte design strategy.

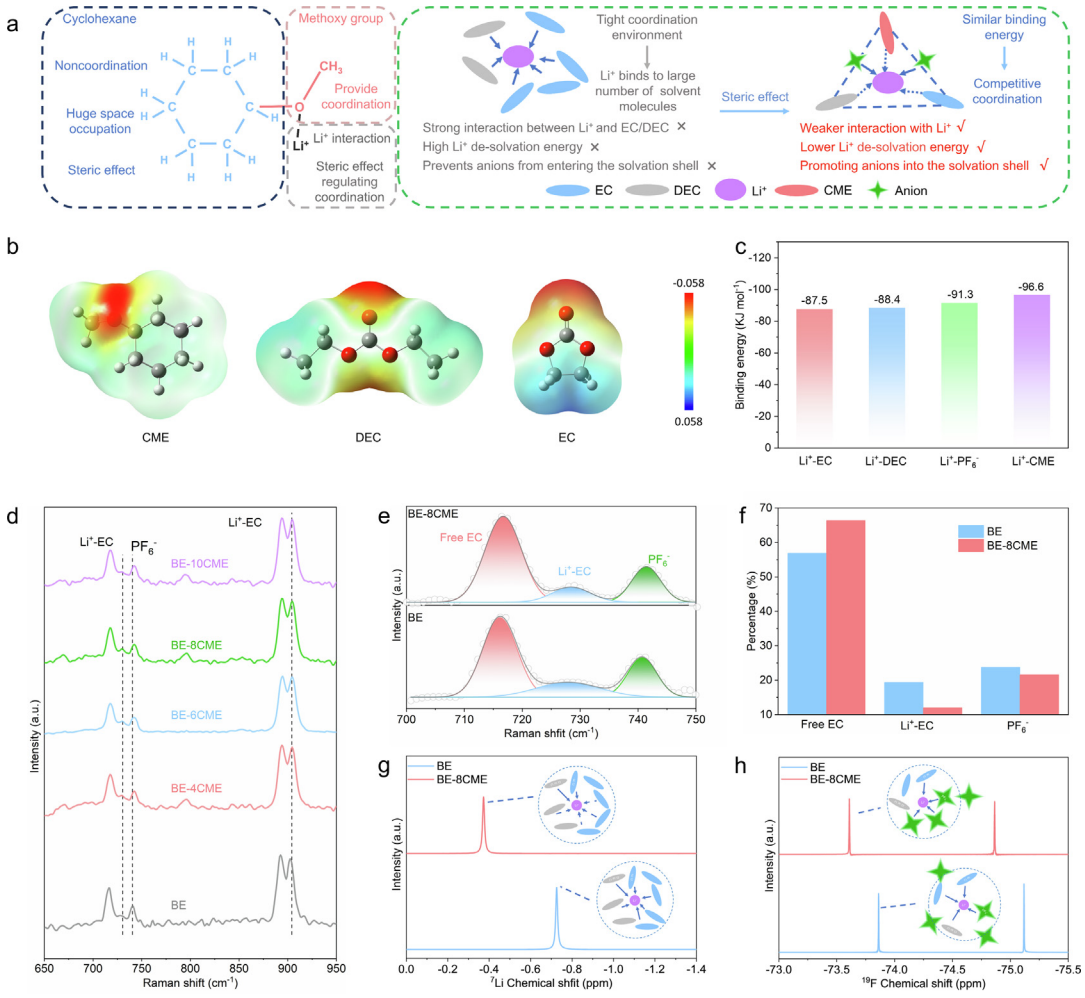

Fig. 2. Characterization of electrolytes. (a) Schematic illustration of the role of CME molecules. (b) Surface electrostatic potentials of CME, DEC and EC. (c) Binding energies of Li^+ with different molecules and ions. (d) Raman spectra of different electrolytes in the range of 650–950 cm^{-1}. (e) Raman spectra of different electrolytes in the range of 700–750 cm^{-1}, along with the deconvoluted constituent peaks (colored). (f) Percentage of the area of the deconvoluted constituent peaks. (g) ^7Li NMR spectra of BE and BE-8CME. (h) ^{19}F NMR spectra of BE and BE-8CME.

single-site oxygen in the CME molecule effectively reduces the coordination between Li^+ and the solvent molecules and increases the possibility of Li^+ and PF_6^- anion coordination. The binding energies of Li^+ and EC, DEC, PF_6^- and CME molecules are shown in Fig. 2c and Fig. S1. The similar binding energies of CME and EC/DEC to Li^+ indicate that CME molecules can enter the solvation sheath of Li^+ [33].

The modulation of Li^+ solvation sheath by CME was further verified using Raman spectroscopy and nuclear magnetic resonance (NMR) analysis. Raman spectra (Fig. 2d) show that the coordination environment of Li^+ changes significantly in the range of 700–760 cm^{-1} with the introduction of CME [34,35]. Specifically, the characteristic peak of PF_6^- shifts from 740.5 to 743 cm^{-1}, indicating enhanced interaction between anions and Li^+. Fig. 2e, f, Fig. S2 and Table S1 present the relative integrated peak areas of different electrolytes in the range of 700–750 cm^{-1}. The intensity of Li^+–EC increases from 19.38% to 23.51% with the addition of 4 wt% CME, possibly due to the homogeneous dispersion of a small amount of CME, making the solvation sheath more compact. As the CME concentration increases to 6 wt%, the intensity of Li^+–EC decreases to 21.74%, while the intensity of PF_6^- increases to 25.54%. At 8 wt% CME, the Li^+–EC intensity further decreases to the lowest value (12.04%), indicating weaker binding of Li to EC and more PF_6^- entering the solvation sheath. The Li^+–EC intensity of BE-8CME (12.04%) is significantly lower than that of BE (19.38%), further confirming the modulation of the solvation sheath of Li^+ by CME. When the CME concentration is increased to 10 wt%, the intensity of Li^+–EC rises to 21.99%, and the intensity of PF_6^- increases slightly (from 21.62% to 22.25%). This may be attributed to the excessive CME occupying the space outside the solvation sheath, making them to become compact, which is not favorable for the Li^+ desolvation. Therefore, BE-8CME was selected for further characterization in subsequent experiments.

The electrolyte BE-8CME was further analyzed by NMR. The ^7Li NMR spectra (Fig. 2g) show that the peaks of BE-8CME shift to a lower field compared with BE, indicating a decrease in the electron cloud density around Li^+ [36]. This result is attributed to the weakened binding of Li^+ to a large number of ECs molecules, resulting in a reduction in the electron cloud density around Li^+. In the ^{19}F NMR spectra (Fig. 2h), the peaks of BE-8CME also exhibit a low-field shift compared with the BE, indicating a decrease in the electron cloud density around PF_6^-, which can be attributed to the enhanced ability of the PF_6^- ion to coordinate with Li^+ [37]. The results of NMR analysis are in consistent with those observed by Raman spectroscopy, further validating the modulation of Li^+ solvation sheath by CME.

The solvation sheath of Li^+ was investigated by molecular dynamics (MD) simulations [38]. Fig. 3a, b illustrate the MD

snapshots of BE and BE-8CME, while Fig. S3 depicts the typical solvation sheaths of the two electrolytes. In BE, the distances between EC and Li^+ are 1.820, 1.985, and 2.049 Å, respectively, the distance between DEC and Li^+ is 1.984 Å. The distance between PF_6^- and Li^+ is 3.562 Å. In BE-CME, the distances between EC and Li^+ increase to 2.052 and 2.074 Å, respectively, and, compared to BE, the distances between Li^+ and EC increases, and DEC and Li^+ are 1.980 Å with less variation. Notably, the distance between Li^+ and PF_6^- decreases significantly to 3.262 Å. The radial distribution function (RDF) of BE-8CME (Fig. 3d) shows a distinct peak at 1.73 Å, indicating that CME enters the first solvation sheath of Li^+. The RDF peaks for EC and DEC appear at 1.95 Å and 1.97 Å, respectively, reflecting their similar binding energies with Li^+.

Fig. 3c, d demonstrate that the steric-hindrance effect of CME leads to a reduction in the coordination peaks of Li^+ with other solvent molecules. Conversely, the local concentration increase caused by the steric-hindrance effect enhances the coordination peaks of Li^+ with PF_6^-. Fig. 3e illustrates the coordination numbers

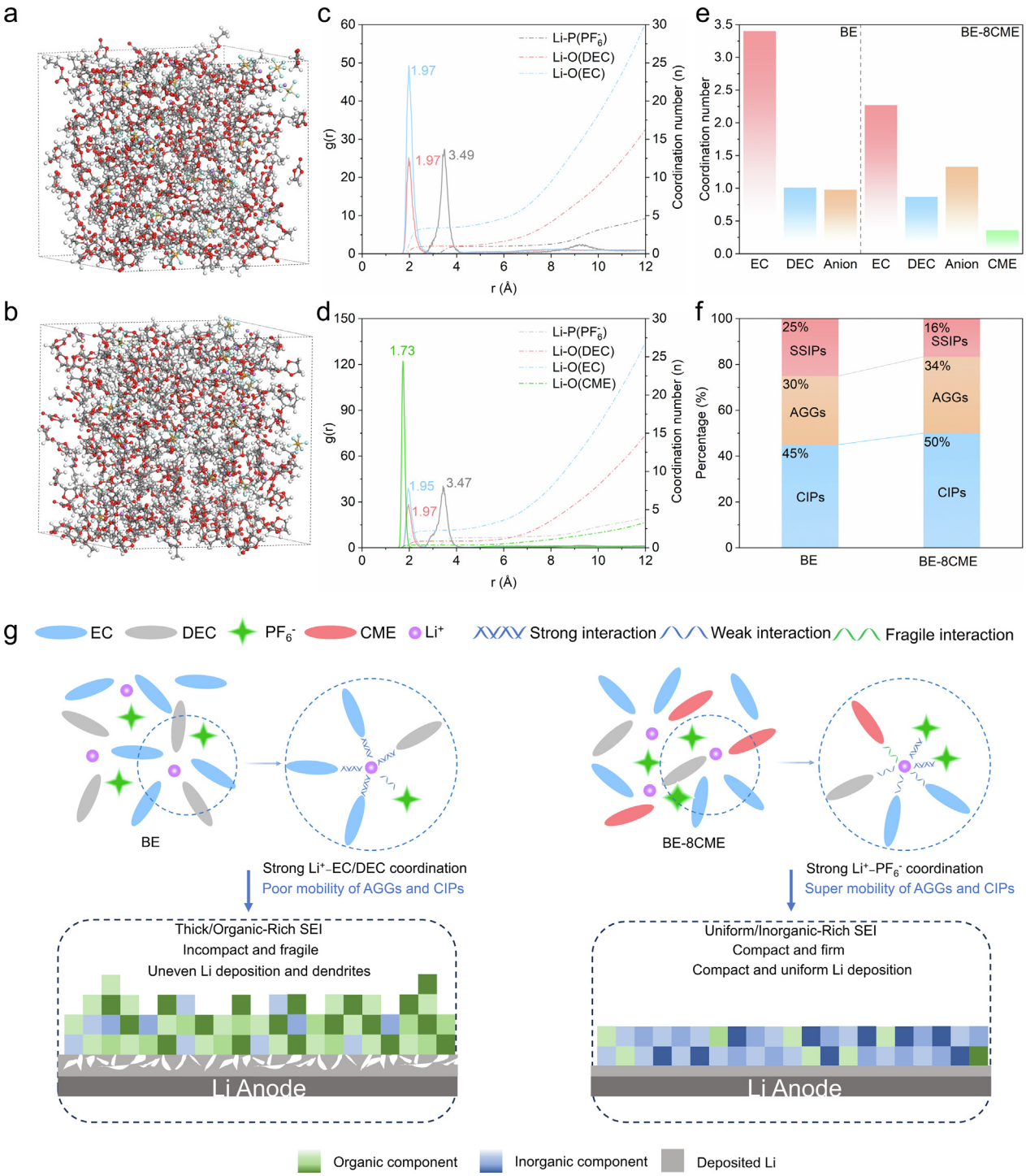

Fig. 3. Solvation sheath of the electrolytes. (a, b) Snapshots of the BE and BE-8CME after MD simulation. (c, d) RDF of BE and BE-8CME after MD simulation. (e) Coordination numbers of the BE and BE-8CME systems. (f) Possible solvation sheath distributions of BE and BE-8CME obtained from MD simulations. (g) Solvation sheath models of the two electrolytes and a schematic illustration of SEI formation.

of Li^+ with each component in BE and BE-8CME. After the addition of CME, the coordination number of Li^+ with DEC decreases from 1.01 to 0.87, and the coordination number of Li^+ with EC decreases from 3.40 to 2.27, primarily due to the steric-hindrance effect of CME. Meanwhile, the coordination number of Li^+ with PF_6^- increases from 0.98 to 1.33, indicating that more PF_6^- anions enter the solvation sheath. In the BE electrolyte, the strong interaction of Li^+ with EC/DEC results in a tight solvation sheath, weakening the binding of Li^+ to PF_6^-. In contrast, in the BE-8CME electrolyte, the steric-hindrance effect of CME attenuates the binding of Li^+ with EC/DEC and promotes more PF_6^- to enter the solvation sheath, leading to an increase in the percentages of AGGs and CIPs from 30% and 45% to 34% and 50%, respectively (Fig. 3f).

Based on the findings from Raman spectroscopy, NMR analysis and theoretical calculations, we propose the following model for Li^+ solvation (Fig. 3g). In BE, strong Li^+–EC/DEC coordination leads to a solvation sheath dominated by solvent molecules, forming a tight and organic-rich solvation sheath. In BE-8CME, the addition of CME loosens the solvation sheath, weakening the solvation ability of the solvent and increasing the number of PF_6^- anions in the solvation sheath. The SEI derived from the tight, solvent-dominated solvation sheath in BE is rich in organic components and inhomogeneous, which tends to promote dendrite growth. In contrast, the anion-rich solvation sheath in BE-8CME is more conducive to the formation of inorganic SEI, resulting in more uniform lithium deposition.

2.2. Properties and kinetics of electrolytes

The intrinsic properties of the BE-8CME electrolyte were comprehensively evaluated by electrochemical characterization and theoretical studies. The addition of 8 wt% CME significantly enhances the ion mobility number of the electrolyte from 0.482 to 0.744 (Fig. 4a). This improvement is attributed to the weakened binding of Li^+ to the solvent molecules [39]. At 25 °C, the ionic conductivity of BE-8CME (4.212 mS cm^{-1}) is notably higher than that of BE (3.059 mS cm^{-1}) (Fig. 4a and Fig. S4), which can be attributed to the enhanced dissociation of lithium salts facilitated by CME [40]. Tafel polarization curves (Fig. 4b) indicate that the introduction of the CME increases the exchange current density (j_0), suggesting enhanced Li^+ transport kinetics. Electrochemical impedance spectroscopy (EIS) of the Li||Li symmetric cell (Fig. S5) reveals that the charge transfer resistance of the BE-8CME electrolyte is lower than that of the BE electrolyte, indicating enhanced Li^+ transport within the SEI layer. The microcurrent exchange cur-

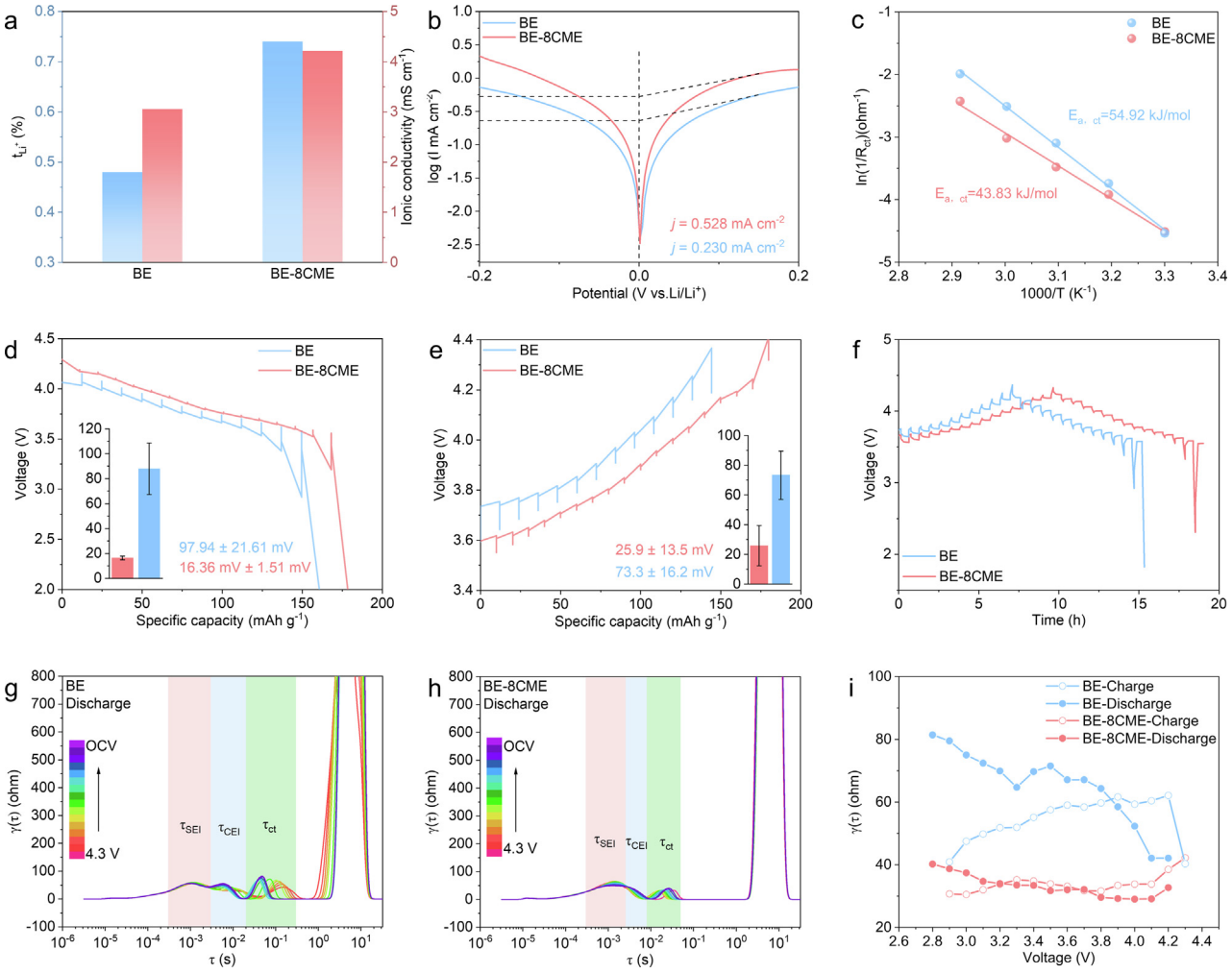

Fig. 4. Electrochemical properties of electrolytes. (a) Ion mobility numbers and ionic conductivity for BE-8CME and BE electrolytes. (b) Tafel curves of Li||Li symmetric cells. (c) $E_{a,ct}$ calculated by fitting EIS data at different temperatures. (d–f) GITT curves of NCM electrodes in BE and BE-8CME at different states of charge. (g, h) DRT results of BE-8CME and BE in discharged state. (i) Variation of peak resistance at τ_{ct} in the range of 10^{-2}–10^{-1} s from DRT analysis.

rent density (Fig. S6) further confirms the enhancement in electrolyte kinetics [41]. Activation energy tests (Fig. 4c) show that BE-8CME has a lower desolvation energy ($E_{a,ct}$ = 43.83 kJ mol^{-1}) compared with BE, indicating more rapid ion transport kinetics [42]. Additionally, the activation energy of Li^+ transport at the Li/-electrolyte interphase is also improved (Fig. S7) [18]. Galvanostatic intermittent titration technique (GITT) tests (Fig. 4d–f) demonstrate that the Li||NCM811 cell using BE-8CME exhibits a higher capacity (>160 mA h g^{-1}), smaller overpotential, and higher diffusion coefficient for D_{Li^+} (Fig. S8). These improvements are attributed to the reduced diffusion resistance and faster desolvation behavior of Li^+ in the electrolyte [43].

To further investigate the interfacial dynamics of the two electrolyte systems on the negative side, the contact angles of BE and BE-8CME on the anode and polypropylene (PP) separator surfaces were measured (Fig. S9). The results showed that the contact angle on the BE-Li surface (28°) is significantly higher than that on the BE-8CME-Li surface (19°). Similarly, the contact angle on the BE-separator surface (38°) is higher than that on the BE-8CME-separator surface (32°). This indicates that BE-8CME has better wettability, enhancing the affinity between the lithium surface and the carbonate electrolyte, and promoting the efficient and uniform of Li^+ transport [44]. In-situ EIS of Li||NCM811 cells was employed to reveal the interfacial dynamics of Li^+ solvation (Fig. S10). The electrode kinetics at different time scales were analyzed using the distribution of relaxation times (DRT) method (Fig. 4g–i and Fig. S11). Four different processes were identified by their respective time constants (τ): Li^+ conduction in the SEI layer (~10^{-3} s), Li^+ conduction in the cathode electrolyte interphase (CEI) layer (~10^{-2} s), interfacial desolvation by Li^+ solvation (~10^{-2}–10^{-1} s), and Li deposition (~10 s). Generally, a smaller τ value indicates faster electrochemical kinetics. For the resistance of SEI (R_{SEI}) at τ_{SEI} and cathode electrolyte interphase (R_{CEI}) at τ_{CEI}, BE-8CME exhibits a more reversible relaxation process compared with BE, suggesting the formation of a stable SEI/CEI layers during cycling. Fig. 4i shows the variation of the peak resistance at τ_{ct} with voltage, and the cell exhibits a decrease in charge transfer resistance (R_{CT}) at τ_{ct}, indicating a lower energy barrier for charge transfer at the interface. These results indicate that Li^+ in the BE-8CME-derived SEI undergoes rapid transport and desolvation, consistent with the weak interaction of solvent molecules with Li^+ in BE-8CME.

2.3. Lithium metal anode stability and interfacial properties

First, the interfacial stability of Li metal was investigated using Li||Li symmetric cells with the two electrolytes. As shown in Fig. 5a, the BE-8CME-based Li||Li cell cycled stably for 500 h at a current density of 1 mA cm^{-2} and a capacity of 0.5 mA h g^{-1}. In contrast, the BE-based Li||Li cell exhibited a gradual increase in overpotential after 300 h, with noticeable interface fluctuations, and short-circuited after 460 h. In addition, the average Coulombic efficiency (CE) of the electrolyte was determined using the modified Aurbach method (Fig. 5b) [45]. The BE-8CME electrolyte achieved a high average CE of 98.17%, superior to the BE electrolyte (81.77%), indicating enhanced stability of the BE-8CME with the Li anode.

To investigate the stability of lithium plating/stripping and the reason for the improved CE, the post-cycling Li||Li cells were disassembled, and the lithium metal surfaces were analyzed using X-ray photoelectron spectroscopy (XPS). The Li 1*s* XPS spectrum (Fig. 5d) shows peaks at 54.8, 55.4, and 56.0 eV, corresponding to LiO_2, Li_2CO_3, and LiF, respectively [33]. In the BE system, the signals of Li_2CO_3 are stronger than those of LiO_2 and LiF, suggesting that solvation sheaths containing a large number of solvent molecules are reduced near the anode, leading to significant electrolyte consumption [46,47]. In contrast, the BE-8CME system forms an inorganic-rich SEI, as evidenced by the strong LiO_2 and LiF band signals. The F 1*s* XPS spectrum (Fig. 5c) shows the LiF signal in BE is significantly weaker than that in BE-8CME [16], attributed to the anion-rich localized solvation structure, with LiF originating from the decomposition of the PF_6^- anion. Previous studies have demonstrated that LiF is a key component in SEI, and LiF-rich SEI can effectively promote uniform Li^+ transport and deposition [48,49]. The C 1*s* XPS (Fig. S12) shows peaks at 284.8, 286.6, 288.1, and 290 eV, corresponding to C—C, C—O, C═O and CO_3^{2-} [23], respectively. The C═O peak of the BE system is slightly higher than that in the BE-8CME system, further indicating a higher content of organic components in the SEI derived from the BE system.

Scanning electron microscopy (SEM) was used to characterize the morphology of lithium deposition. In the BE system, lithium deposition was inhomogeneous, loose, and porous (Fig. 5e), leading to persistent dendrite growth and severe interfacial reactions. In contrast, lithium deposition in BE-8CME system was uniform and dense (Fig. 5g), mitigating parasitic reactions and the formation of "dead" lithium. Meanwhile, the thickness of lithium deposition in BE-8CME was only 25.98 μm, significantly thinner than that in the BE electrolyte (73.83 μm) (Fig. 5f–h). In-situ optical microscopy visually assessed the electrolyte's effect on lithium deposition (Fig. 5i, j and Fig. S13). Optical images of BE and BE-8CME electrolytes at a current density of 1 mA cm^{-2} at 0, 2, 4, 6, 8, and 10 min of deposition show that the BE electrolyte began to form visible Li dendrites at 2 min, followed by rapid growth. In contrast, no significant Li dendrite growth was observed in the BE-8CME electrolyte, indicating uniform and dense Li deposition, consistent with the SEM cross-section analysis. The anion-rich solvation sheath and lower desolvation barrier in the BE-8CME electrolyte facilitated uniform and dense Li deposition, preventing dendrite growth. Finally, atomic force microscopy (AFM) confirmed that the surface roughness of the cycled lithium in BE-8CME (Roughness = 35.5 nm) was significantly lower than that in BE (Roughness = 68.1 nm), further corroborating the benefits of the optimized formulation.

2.4. Li||$LiNi_{0.8}Co_{0.1}Mn_{0.1}O_2$ cell electrochemical properties

Given the excellent lithium-metal interfacial compatibility and anode stability of BE-8CME electrolyte, we applied it to Li||$LiNi_{0.8}Co_{0.1}Mn_{0.1}O_2$ (NCM811) batteries. Prior to long-cycle testing, all cells underwent several activation cycles at a low rate (0.1 C). As shown in Fig. 6a and Fig. S14, the long-term stability of the battery using the BE-8CME electrolyte was significantly superior to that of the BE electrolyte at 1 C. The battery with BE electrolyte experienced rapid capacity decay within the first 100 cycles, retaining only 80% of its initial capacity after 171 cycles. In contrast, the battery with BE-8CME electrolyte exhibited significant capacity decay only after 200 cycles, retaining 82% of its initial capacity after 463 cycles, with a CE of 99.45%. Fig. S15 shows the cycle performance of the Li||NCM811 battery with N/P = 1.6. The BE-8CME demonstrates superior performance at a low N/P ratio. As illustrated in Fig. 6b, c, the capacities of Li||NCM811 battery with BE-8CME electrolyte were 197.8, 196.7, 191.0, 181.3, 171.6, and 150.8 mA h g^{-1} at 0.1, 0.2, 0.5, 1, 2, and 5 C, respec-

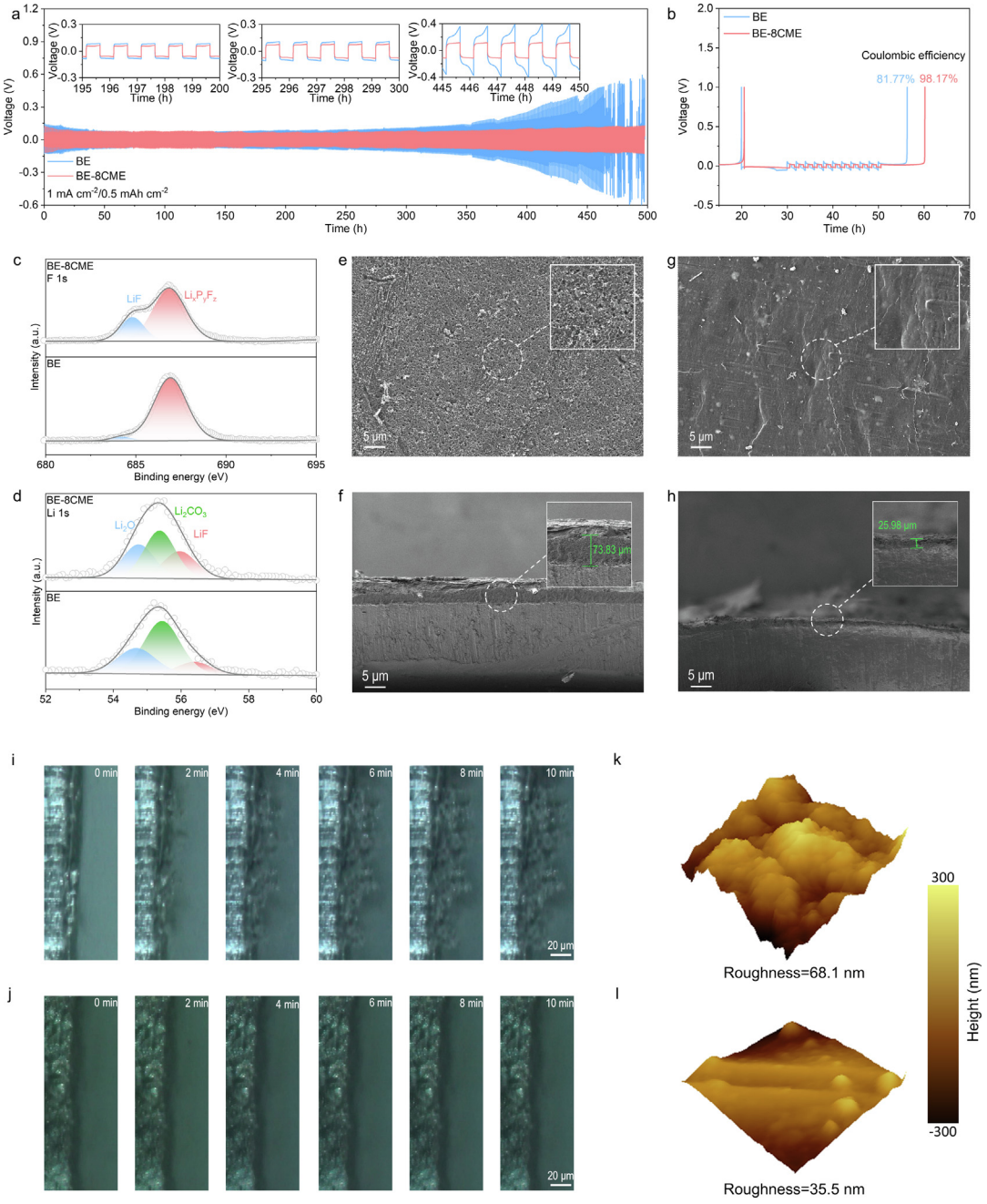

Fig. 5. Stabilization and interfacial properties of electrolytes on lithium metal anode. (a) Cycling performance of Li||Li symmetric cell. (b) CE of Li||Cu cells tested using the Aurbach method. (c, d) F 1*s* and Li 1*s* XPS spectra of the lithium anode surface after cycling. SEM images of Li deposition in (e, f) BE and (g, h) BE-8CME electrolytes. In-situ optical images of lithium deposition in (i) BE and (j) BE-8CME. AFM images of the lithium metal surface after cycling in (k) BE and (l) BE-8CME electrolytes.

tively, and recovered to 198.6 mA h g^{-1}, indicating superior interfacial kinetic behavior under various current densities.

Further, the cycling performance of the Li||NCM811 batteries was evaluated at a high rate of 5 C. As shown in Fig. 6d–f, the battery with BE-8CME electrolyte retained 80% of its capacity after 173 cycles. In comparison, the battery with BE electrolyte showed rapid capacity decay from the beginning, with capacity retention dropping to 80% after just 27 cycles. After 200 cycles, the capacity retention of the battery using BE-8CME electrolyte was 66.04%, whereas the battery with BE electrolyte had a capacity retention of less than 60%. In summary, the long-term stability and fast-charging performance of the Li||NCM811 battery with BE-8CME electrolyte can be attributed to two key factors: (i) the steric-hindrance effect of CME, which weakens the binding of Li^+ with solvent molecules, thereby facilitating the desolvation of Li^+; and (ii) the anion-rich solvation sheath, which effectively stabilizes the lithium-anode interface and inhibits the growth of lithium dendrites and harmful side reactions. As shown in Fig. 6g, compared with the previously reported work, the Li||NCM811 batteries with the optimized formulations in this study demonstrated outstanding performance in terms of fast-charging capability (5 C), cycling stability (173 cycles), and capacity retention (80%). These results highlight the excellent application potential of the optimized electrolyte [50–57].

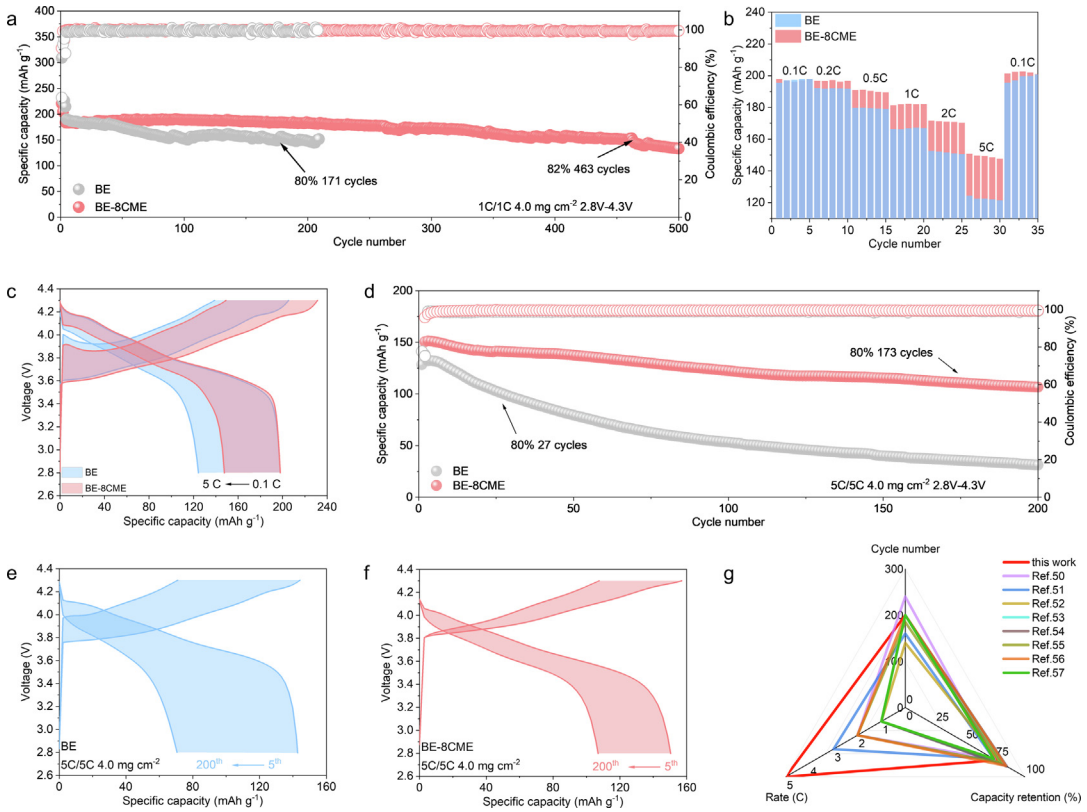

Fig. 6. Performance of Li||NCM811 batteries. (a) Cycling performance of Li||NCM811 batteries at 1 C. (b, c) Rate performance of Li||NCM811 batteries. (d–f) Cycling performance of Li||NCM811 batteries at a high rate of 5 C. (g) Comparison of the fast charge/discharge and cycling performance of this study with other reported data.

3. Conclusions

In this work, the solvation sheath of Li^+ is optimized by incorporating the macromolecular steric effect of CME, which significantly enhances the electrolyte capabilities in fast charge/discharge and long-cycle performance. The steric-hindrance effect of CME reduces the coordination of Li^+ with the original solvent molecules (EC and DEC), while promoting the coordination of Li^+ with the PF_6^- anion. This results in faster ion transport and desolvation kinetics. Additionally, the optimized electrolyte formulation facilitates the formation of a stable, anion-derived, inorganic-rich SEI, which significantly improves the interfacial stability of lithium metal electrodes. As a result, the Li||NCM811 battery with the modified electrolyte retains 82% of its initial capacity after 463 cycles at 1 C. Moreover, the battery maintains 80% capacity retention after 173 cycles under extreme fast-charging conditions at 5 C. These results not only validate the effectiveness of regulating the electrolyte properties through the effect of steric hindrance, but also provide solution for realizing fast charging and stable cycling lithium metal batteries.

Experimental section

Experimental details can be found in the Supporting Information.

CRediT authorship contribution statement

Ruizhe Xu: Writing – original draft, Visualization, Methodology, Conceptualization. **Anjun Hu:** Visualization, Conceptualization. **Zhen Wang:** Visualization, Conceptualization. **Kai Chen:** Writing – review & editing, Investigation. **Jingze Chen:** Validation, Formal analysis. **Wang Xu:** Validation, Formal analysis. **Gang Wu:** Formal analysis. **Fei Li:** Formal analysis. **Jian Wang:** Validation. **Jianping Long:** Writing – review & editing, Supervision, Project administration, Funding acquisition.

Declaration of competing interest

The authors declare that they have no known competing financial interests or personal relationships that could have appeared to influence the work reported in this paper.

Acknowledgements

This work was supported by the Lithium Resources and Lithium Materials Key Laboratory of Sichuan Province (LRMKF202405), the National Natural Science Foundation of China (52402226), the Natural Science Foundation of Sichuan Province (2024NSFSC1016), and the Scientific Research Startup Foundation of Chengdu University of Technology (10912-KYQD2023-10240) as well as the opening funding from Key Laboratory of Engineering Dielectrics and Its Application (Harbin University of Science and Technology) (KFM202507, Ministry of Education). Dr. Jian Wang also acknowledges the funding provided by the Alexander von Humboldt Foundation. We would like to thank Mr Li Julong from Shiyanjia Lab (www.shiyanjia.com) for the support of XPS analysis and SCI-GO (www.sci-go.com) for the support of Raman analysis. And we appreciate Phadcalc (www.phadcalc.com) for the molecular dynamics simulation.

Appendix A. Supplementary material

Supplementary data to this article can be found online at https://doi.org/10.1016/j.jechem.2025.01.038.

References

[1] G.M. Hobold, C. Wang, K. Steinberg, Y. Li, B.M. Gallant, Nat. Energy 9 (2024) 580–591.
[2] J. Pokharel, A. Cresce, B. Pant, M.Y. Yang, A. Gurung, W. He, A. Baniya, B.S. Lamsal, Z. Yang, S. Gent, X. Xian, Y. Cao, W.A. Goddard, K. Xu, Y. Zhou, Nat. Commun. 15 (2024) 3085.
[3] Q.-S. Liu, Y.-Z. Quan, M.-C. Liu, G.-R. Zhu, X.-L. Wang, G. Wu, Y.-Z. Wang, J. Energy Chem. 83 (2023) 239–246.
[4] W. Li, E.M. Erickson, A. Manthiram, Nat. Energy 5 (2020) 26–34.
[5] Z. Cui, Z. Jia, D. Ruan, Q. Nian, J. Fan, S. Chen, Z. He, D. Wang, J. Jiang, J. Ma, X. Ou, S. Jiao, Q. Wang, X. Ren, Nat. Commun. 15 (2024) 2033.
[6] A. Hu, W. Chen, F. Li, M. He, D. Chen, Y. Li, J. Zhu, Y. Yan, J. Long, Y. Hu, T. Lei, B. Li, X. Wang, J. Xiong, Adv. Mater. 35 (2023) 2304762.
[7] B. Yang, A. Hu, T. Li, K. Li, Y. Li, J. Jiang, Z. Xiao, Z.W. Seh, J. Long, Energy Storage Mater. 70 (2024) 103512.
[8] K. Li, Z. Wang, B. Yang, T. Li, B. Li, J. Chen, Z. Yan, M. He, A. Hu, J. Long, Chem. Eng. J. 493 (2024) 152527.
[9] T. Li, K. Chen, B. Yang, K. Li, B. Li, M. He, L. Yang, A. Hu, J. Long, Chem. Sci. 15 (2024) 12108–12117.
[10] J. Wang, J. Zhang, Y. Zhang, H. Li, P. Chen, C. You, M. Liu, H. Lin, S. Passerini, Adv. Mater. 36 (2024) 2402792.
[11] G.-R. Zhu, Q. Zhang, Q.-S. Liu, Q.-Y. Bai, Y.-Z. Quan, Y. Gao, G. Wu, Y.-Z. Wang, Nat. Commun. 14 (2023) 4617.
[12] Q.-K. Zhang, X.-Q. Zhang, J. Wan, N. Yao, T.-L. Song, J. Xie, L.-P. Hou, M.-Y. Zhou, X. Chen, B.-Q. Li, R. Wen, H.-J. Peng, Q. Zhang, J.-Q. Huang, Nat. Energy 8 (2023) 725–735.
[13] Y.-H. Tan, Z. Liu, J.-H. Zheng, Z.-J. Ju, X.-Y. He, W. Hao, Y.-C. Wu, W.-S. Xu, H.-J. Zhang, G.-Q. Li, L.-S. Zhou, F. Zhou, X. Tao, H.-B. Yao, Z. Liang, Adv. Mater. 36 (2024) 2404815.
[14] H. Cheng, Q. Sun, L. Li, Y. Zou, Y. Wang, T. Cai, F. Zhao, G. Liu, Z. Ma, W. Wahyudi, Q. Li, J. Ming, ACS Energy Lett. 7 (2022) 490–513.
[15] J. Holoubek, Y. Yin, M. Li, M. Yu, Y.S. Meng, P. Liu, Z. Chen, Angew. Chem. Int. Ed. 58 (2019) 18892–18897.
[16] Z. Cui, C. Liu, A. Manthiram, Adv. Mater. 36 (2024) 2409272.
[17] H. Wang, Z. Yu, X. Kong, S.C. Kim, D.T. Boyle, J. Qin, Z. Bao, Y. Cui, Joule 6 (2022) 588–616.
[18] Y. Lu, W. Zhang, S. Liu, Q. Cao, S. Yan, H. Liu, W. Hou, P. Zhou, X. Song, Y. Ou, Y. Li, K. Liu, ACS Nano 17 (2023) 9586–9599.
[19] L. Zhao, Z. Wu, Z. Wang, Z. Bai, W. Sun, K. Sun, ACS Nano 16 (2022) 20891–20901.
[20] J. Wang, J. Zhang, J. Wu, M. Huang, L. Jia, L. Li, Y. Zhang, H. Hu, F. Liu, Q. Guan, M. Liu, H. Adenusi, H. Lin, S. Passerini, Adv. Mater. 35 (2023) 2302828.
[21] Y. Cai, Y. Hou, Y. Lu, Q. Zhang, Z. Yan, J. Chen, Angew. Chem. Int. Ed. 62 (2023) e202218014.
[22] S. Chen, J. Fan, Z. Cui, L. Tan, D. Ruan, X. Zhao, J. Jiang, S. Jiao, X. Ren, Angew. Chem. Int. Ed. 62 (2023) e202219310.
[23] X. Huang, R. Li, C. Sun, H. Zhang, S. Zhang, L. Lv, Y. Huang, L. Fan, L. Chen, M. Noked, X. Fan, ACS Energy Lett. 7 (2022) 3947–3957.
[24] Y. Zhao, Z. Hu, Z. Zhao, X. Chen, S. Zhang, J. Gao, J. Luo, J. Am. Chem. Soc. 145 (2023) 22184–22193.
[25] D.J. Kautz, X. Cao, P. Gao, B.E. Matthews, Y. Xu, K.S. Han, F. Omenya, M.H. Engelhard, H. Jia, C. Wang, J. Zhang, W. Xu, Adv. Energy Mater. 13 (2023) 2301199.
[26] P. Liang, H. Hu, Y. Dong, Z. Wang, K. Liu, G. Ding, F. Cheng, Adv. Funct. Mater. 34 (2024) 2309858.
[27] M. Qin, Z. Zeng, F. Ma, C. Gu, X. Chen, S. Cheng, J. Xie, ACS Energy Lett. 9 (2024) 2536–2544.
[28] J. Wang, L. Xie, W. Wu, Y. Liang, M. Cao, C. Gao, Y. Bo, J. Zhang, J. Zhang, Energy Environ. Sci. 17 (2024) 9100–9111.
[29] F. Cheng, W. Zhang, Q. Li, C. Fang, J. Han, Y. Huang, ACS Nano 17 (2023) 24259–24267.
[30] S.C. Kim, J. Wang, R. Xu, P. Zhang, Y. Chen, Z. Huang, Y. Yang, Z. Yu, S.T. Oyakhire, W. Zhang, L.C. Greenburg, M.S. Kim, D.T. Boyle, P. Sayavong, Y. Ye, J. Qin, Z. Bao, Y. Cui, Nat. Energy 8 (2023) 814–826.
[31] J. Lee, A.-R. Jeon, H.J. Lee, U. Shin, Y. Yoo, H.-D. Lim, C. Han, H. Lee, Y.J. Kim, J. Baek, D.-H. Seo, M. Lee, Energy Environ. Sci. 16 (2023) 2924–2933.
[32] Y. Chen, Q. He, Y. Zhao, W. Zhou, P. Xiao, P. Gao, N. Tavajohi, J. Tu, B. Li, X. He, L. Xing, X. Fan, J. Liu, Nat. Commun. 14 (2023) 8326.
[33] R. Jia, H. Dai, X. Tu, C. Sun, S. Sun, C. Lai, Adv. Energy Mater. 13 (2023) 2302747.
[34] X. Wang, L. Yang, N. Ahmad, L. Ran, R. Shao, W. Yang, Adv. Mater. 35 (2023) 2209140.
[35] L.-Y. Huang, Y.-C. Shih, S.-H. Wang, P.-L. Kuo, H. Teng, J. Mater. Chem. A 2 (2014) 10492–10501.
[36] C. Yan, Y. Yao, X. Chen, X. Cheng, X. Zhang, J. Huang, Q. Zhang, Angew. Chem. Int. Ed. 57 (2018) 14055–14059.
[37] Y. Zou, G. Liu, Y. Wang, Q. Li, Z. Ma, D. Yin, Y. Liang, Z. Cao, L. Cavallo, H. Kim, L. Wang, H.N. Alshareef, Y. Sun, J. Ming, Adv. Energy Mater. 13 (2023) 2300443.
[38] S. Zhang, S. Li, X. Wang, C. Li, Y. Liu, H. Cheng, S. Mao, Q. Wu, Z. Shen, J. Mao, H. Pan, Y. Lu, Nano Energy 114 (2023) 108639.
[39] P. Zhou, X. Zhang, Y. Xiang, K. Liu, Nano Res. 16 (2023) 8055–8071.
[40] B. Koo, H. Lee, S. Hwang, J. Lee, Y.-K. Han, K.H. Ahn, C. Lee, H. Lee, J. Phys. Chem. C 127 (2023) 18271–18278.
[41] J. Wu, Z. Gao, Y. Tian, Y. Zhao, Y. Lin, K. Wang, H. Guo, Y. Pan, X. Wang, F. Kang, N. Tavajohi, X. Fan, B. Li, Adv. Mater. 35 (2023) 2303347.
[42] X. Huang, M. Wang, Y. Zhou, C. Shi, Z. Li, B. Hong, J. Li, Y. Lai, Nano Energy 129 (2024) 110031.
[43] Y. Gao, G. Wu, W. Fang, Z. Qin, T. Zhang, J. Yan, Y. Zhong, N. Zhang, G. Chen, Angew. Chem. Int. Ed. 63 (2024) e202403668.
[44] J. Zhang, J. Iocozzia, J. Huang, K. Meng, Y. Lai, Z. Lin, Energy Environ. Sci. 11 (2024) 772–799.
[45] Y. Zhao, T. Zhou, M. Mensi, J.W. Choi, A. Coskun, Nat. Commun. 14 (2023) 299.
[46] B. Jagger, M. Pasta, Joule 7 (2023) 2228–2244.
[47] E.W.C. Spotte-Smith, R.L. Kam, D. Barter, X. Xie, T. Hou, S. Dwaraknath, S.M. Blau, K.A. Persson, ACS Energy Lett. 7 (2022) 1446–1453.
[48] A. Hu, W. Chen, X. Du, Y. Hu, T. Lei, H. Wang, L. Xue, Y. Li, H. Sun, Y. Yan, J. Long, C. Shu, J. Zhu, B. Li, X. Wang, J. Xiong, Energy Environ. Sci. 14 (2021) 4115–4124.
[49] X. Fan, J. Zhang, N. Yao, J. Chen, X. Chen, L. Kong, Adv. Energy Mater. 14 (2024) 2303336.
[50] X. Zhang, Y. Wang, Z. Ouyang, S. Wang, X. Zhao, Q. Xu, B. Yuan, X. Yue, Z. Liang, S. Geng, S. Tang, H. Sun, Adv. Energy Mater. 14 (2024) 2303048.
[51] T. Yang, L. Li, J. Zou, Y. Yao, Q. Zhang, Z. Jiang, Y. Li, Adv. Funct. Mater. 34 (2024) 2404945.
[52] Z. Wu, C. Wang, Z. Hui, H. Liu, S. Wang, S. Yu, X. Xing, J. Holoubek, Q. Miao, H.L. Xin, P. Liu, Nat. Energy 8 (2023) 340–350.
[53] P. Xu, Y. Gao, Y. Huang, Z. Shuang, W. Kong, X. Huang, W. Huang, N. Yao, X. Chen, H. Yuan, C. Zhao, J. Huang, Q. Zhang, Adv. Mater. 36 (2024) 2409489.
[54] H. Su, P. Liu, Y. Liu, S. Liu, Y. Zhong, X. Xia, X. Wang, J. Tu, Nano Energy 115 (2023) 108722.
[55] M.M. Rahman, S. Tan, Y. Yang, H. Zhong, S. Ghose, I. Waluyo, A. Hunt, L. Ma, X.-Q. Yang, E. Hu, Nat. Commun. 14 (2023) 8414.
[56] R. Qiao, Y. Zhao, S. Zhou, H. Zhang, F. Liu, T. Zhou, B. Sun, H. Fan, C. Li, Y. Zhang, F. Liu, X. Ding, J. Wook Choi, A. Coskun, J. Song, Chem 11 (2025) 102306.
[57] F. Li, J. Liu, J. He, Y. Hou, H. Wang, D. Wu, J. Huang, J. Ma, Angew. Chem. Int. Ed. 61 (2022) e202205091.